

# Nonlinear Dynamic Modeling for Smart Material Electro-Hydraulic Actuator Development

John P. Larson and Marcelo J. Dapino

Smart Vehicle Concepts Center, Department of Mechanical and Aerospace Engineering  
The Ohio State University, Columbus, OH 43210

## ABSTRACT

Smart material electro-hydraulic actuators use hydraulic rectification by one-way check valves to amplify the motion of smart materials, such as magnetostrictives and piezoelectrics, in order to create compact, lightweight actuators. A piston pump driven by a smart material is combined with a hydraulic cylinder to form a self-contained, power-by-wire actuator that can be used in place of a conventional hydraulic system without the need for hydraulic lines and a centralized pump. The performance of an experimental actuator driven by a 12.7 mm diameter, 114 mm length Terfenol-D rod is evaluated over a range of applied input frequencies, loads, and currents. The peak performance achieved is 37 W, moving a 220 N load at a rate of 17 cm/s and producing a blocked pressure of 12.5 MPa. Additional tests are conducted to quantify the dynamic behavior of the one-way reed valves using a scanning laser vibrometer to identify the frequency response of the reeds and the effect of the valve seat and fluid mass loading. A lumped-parameter model is developed for the system that includes valve inertia and fluid response nonlinearities, and the model results are compared with the experimental data.

**Keywords:** Terfenol-D, magnetostrictive pump, reed valves, hydraulic rectification, electro-hydraulic actuator, fluid added mass, cantilever beam

## 1. INTRODUCTION AND BACKGROUND

The high energy density of the magnetostrictive material Terfenol-D (14-25 kJ/m<sup>3</sup>) makes it an ideal candidate for actuator development.<sup>1</sup> However, the use of this material in certain applications has been limited due to the relatively small displacement that it generates ( $\sim 0.1\%$  strain). Smart material electro-hydraulic actuators (EHAs) use fluid rectification via one-way check valves to transform the high-frequency vibrations of a smart material into large motions of a hydraulic cylinder.

The actuator principle of operation is shown in Figure 1. An applied magnetic field, typically sinusoidal, causes a Terfenol-D rod to alternatively extend and contract. The extension stroke compresses hydraulic fluid in the pump chamber; the pressure in the pumping chamber increases until the outlet check valve opens to allow fluid to flow and cause the output hydraulic cylinder to move. As the piston retracts for the return stroke, the outlet check valve closes, holding the high-side hydraulic cylinder pressure and the cylinder position. The pressure in the pumping chamber continues to decrease until it is below the low-pressure side of the hydraulic cylinder. Then, the inlet check valve opens to draw fluid into the pumping chamber to refill it for the next compression stroke. Although not shown in Figure 1 motion reversal is possible through the addition of a four-way directional control valve. Terfenol-D is a brittle material that is weak in tension, so an accumulator on the low-pressure side of the hydraulic cylinder maintains a bias pressure to keep the smart material driver in compression during operation and to prevent fluid cavitation. The electro-hydraulic actuator concept can also be used to amplify the motion of other smart materials, such as piezoelectrics and electrostrictives, which also produce limited displacements but have a high frequency bandwidth. The resulting system forms a self-contained, power-by-wire hydraulic actuator. Compared to conventional hydraulic systems, which include a centralized pump and associated lines to distribute the fluid, a power-by-wire system has the potential to both reduce weight and improve reliability.

---

Further author information: (Send correspondence to M.J.D.)

M.J.D.: E-mail: dapino.1@osu.edu, Telephone: 1-614-688-3689

J.P.L.: E-mail: larson.303@osu.edu, Telephone: 1-614-247-7480

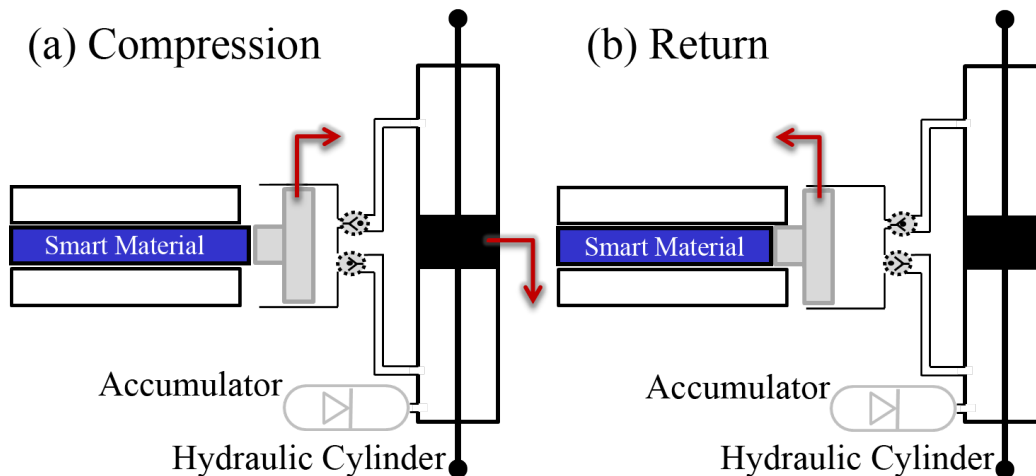


Figure 1. The principle of operation for a smart material electro-hydraulic actuator consists of alternating compression (a) and return (b) strokes of the smart material driver resulting in motion of the hydraulic cylinder.

As the available power output increases with frequency, the general trend for the development of smart material electro-hydraulic actuators has been to increase the power output along with the input frequency of peak operation (Table 1). However, the frequency at which peak performance occurs has been limited to a few hundred hertz even though driver materials are capable of much higher frequencies. For example, Bridger et. al. demonstrated the generation of very high pressures at 2400 Hz, although flow rectification was not shown.<sup>2</sup>

Table 1. Performance comparison of smart material electro-hydraulic actuators.

Blocked Pressure [kPa]	No-Load Flowrate [cm <sup>3</sup> /s]	Power Output [W]	Input Frequency [Hz]	Author	Year
4200*	17*	18.4	225	Larson and Dapino <sup>3</sup>	2012
490*	43*	5.2**	400	Chaudhuri and Wereley <sup>4</sup>	2010
550	19	2.6	200	Kim and Wang <sup>5</sup>	2010
610*	26*	2.5	400	John et al. <sup>6</sup>	2007
7600	4.6*	8.7**	165	Rupinsky and Dapino <sup>7</sup>	2006
2000*	3.7*	3.6	140	Tan et al. <sup>8</sup>	2005
21000	—	—	2400	Bridger et al. <sup>2</sup>	2004
8300	0.34	0.7**	100	Lee et al. <sup>9</sup>	2004
1600*	3.0*	1.2**	300	Sirohi and Chopra <sup>10</sup>	2003
4000	4.2	4.2**	80	Oates and Lynch <sup>11</sup>	2001
4300*	4.6*	4.9**	60	Mauck and Lynch <sup>12</sup>	2000
34	30	0.3**	35	Gerver et al. <sup>13</sup>	1998

\*Value calculated based on the reported blocked-force or no-load velocity values and the output cylinder area.

\*\*Estimate of power output based on the no-load flow rate and blocked pressure.

## 2. PERFORMANCE TESTING

The performance of a magnetostrictive hydraulic actuator was evaluated using the test setup shown in Figure 2. The system uses a 114-mm-long, 13-mm-diameter Terfenol-D rod to drive the pumping piston. A sinusoidal current of 20 A<sub>pk-pk</sub> was applied over a range of input frequencies from 100 Hz to 1200 Hz, with a bias DC

current applied to prevent frequency doubling by the magnetostrictive material. A bias pressure of 2.6 MPa (375 psi) was applied using a nitrogen-charged accumulator keeps the Terfenol-D rod in compression during operation and to favorably align the magnetic domains of the material for peak performance. The hydraulic fluid used was Mobil DTE-24, which has a density of  $871 \text{ kg/m}^3$  at a viscosity of 80 cSt at room temperature.

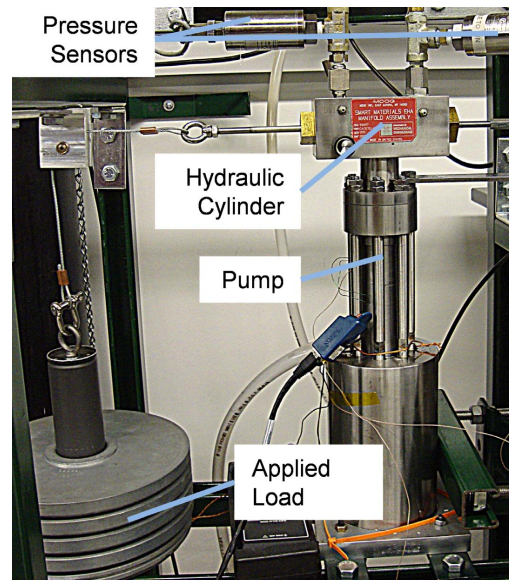


Figure 2. Experimental magnetostrictive-hydraulic actuator configuration; the system was tested over a range of loads using the weight and pulley system shown.

An AE Techtron LVC 5050 linear amplifier was used to apply the input current to the system, and the displacement of the output cylinder was measured using a string potentiometer. A strain gage was used to measure the strain of the Terfenol-D rod during testing. Two thermocouples were used to measure the temperature of the rod and input coil, which was restricted to between 21 and 26 degrees C to avoid variation in the actuator performance due to temperature. Two Sensotec TJE-5000 pressure sensors were provided to measure the pressure at the high-pressure and low-pressure sides of the output cylinder. However, previous test results have shown that the extra volume associated with the high-pressure side sensor passage reduced the system performance, so the passage and sensor were closed off from the rest of the system using a needle valve.<sup>3</sup> A National Instruments cDAQ-9178 was used to collect the sensor data from the experimental system and to generate the sinusoidal input signal applied to the drive coil.

The measured output velocity over the range of applied sinusoidal input current frequencies is shown in Figure 3. The results show a double-peaked output profile with peaks at approximately 225 and 900 Hz. Two interesting features of the output response are the approximately linear response with input frequency below 200 Hz and the high frequency peak, which shows an increase in the location of the peak as the load is increased. Figure 4 shows the output behavior over a larger range of loads at 225 Hz; the response shows a peak no-load velocity of 19 cm/s and a blocked force value of approximately 500 N with a nearly linear response in between. The peak output power of 21 W was measured at 220 N.

Additional tests were conducted at the peak power conditions (225 Hz, 220 N load) using a higher range of input currents (Figure 5). Increasing the input current to  $35 A_{pk-pk}$  increased the output velocity up to 17 cm/s, which corresponds to a power output of 37 W. There is a decrease in efficiency with the increased input current from 12% in the  $20 A_{pk-pk}$  input case to approximately 5% with a  $35 A_{pk-pk}$  input. The decrease in efficiency is due to the Terfenol-D driver approaching saturation, where the amount of strain output for a given applied field decreases. The blocked pressure differential produced by the pump at the  $35 A_{pk-pk}$  current level was also measured at 12.5 MPa.

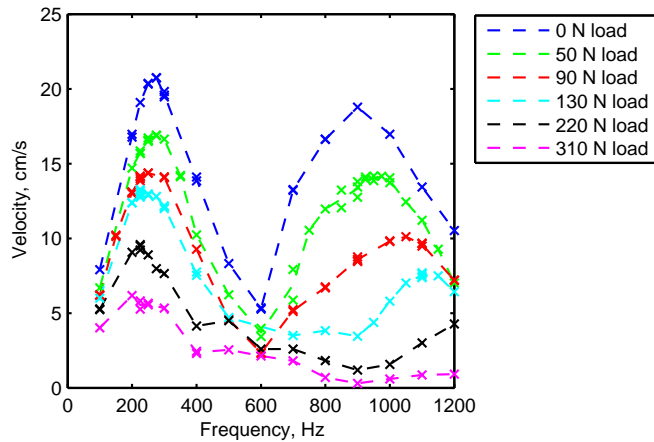


Figure 3. Experimental output cylinder flow rate vs. input frequency with a 20 A<sub>pk-pk</sub> sinusoidal input current applied over the frequency range.

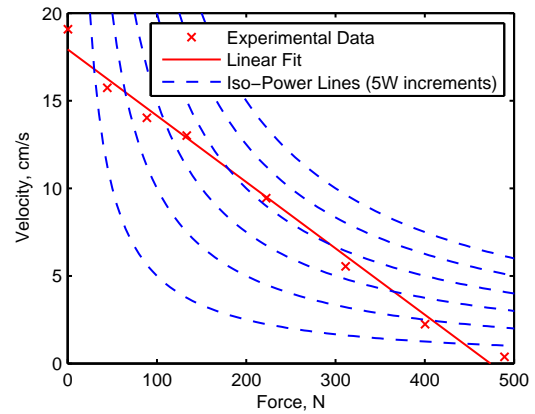


Figure 4. Output force vs. velocity measured at 225 Hz input frequency; the peak output power of 21 W occurs at 220 N applied load.

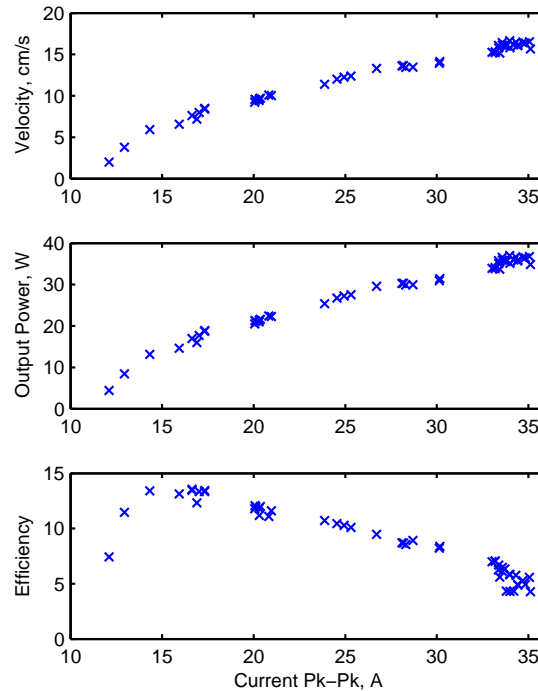


Figure 5. Testing of the experimental actuator at 225 Hz with a 220 N load applied over a range of input frequencies.

## 2.1 Ideal Flow

The approximately linear force-velocity relationship that was demonstrated experimentally (Figure 4) is a direct result of the force-displacement behavior of the material, which can be approximated using the linear piezomagnetic equation

$$\epsilon = s^H \sigma + qH, \quad (1)$$

where the strain  $\epsilon$  is the result of the applied stress  $\sigma$  and magnetic field  $H$ . The coefficient  $s^H$  is the compliance at constant field and  $q$  is the magneto-elastic coupling coefficient. The ideal (loss-less) flow rate  $Q$  as a result

of the strain calculated in (1) is simply product of volume resulting from each strain cycle  $\Delta V$  and the input frequency  $f$  (Figure 6).

$$Q_{\text{ideal}} = \Delta V f = (\epsilon L_{\text{TD}} A_{\text{ch}}) f, \quad (2)$$

where  $L_{\text{TD}}$  and  $A_{\text{ch}}$  respectively denote the length of the Terfenol-D driver and the area of the pumping chamber.

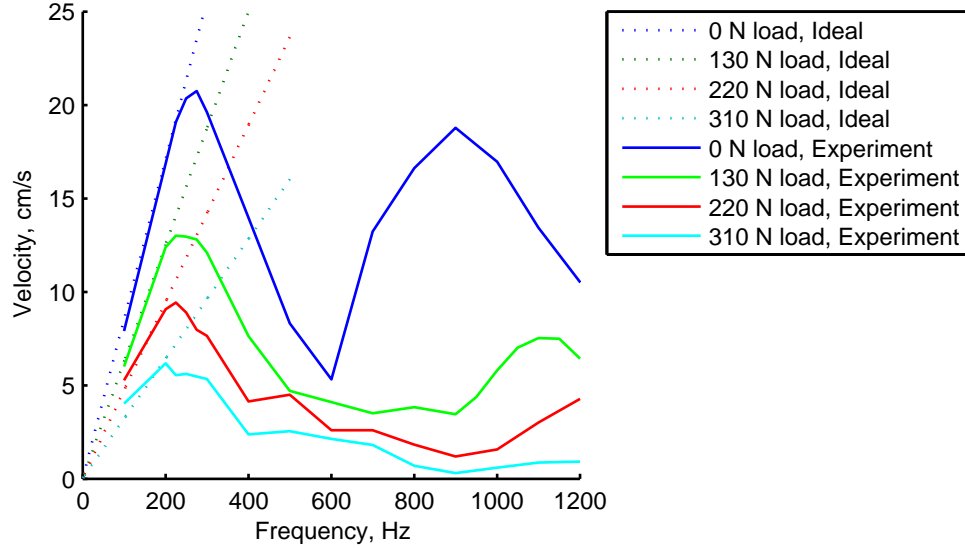


Figure 6. Ideal (loss-less) flow estimate from the linear piezomagnetic equations compared to the experimental results; this linear relationship holds for low frequencies (below  $\sim 200$  Hz).

### 3. MODELING

A lumped-parameter approach is used to develop a model of the overall system. Component-level models are developed for the mechanical and fluid components of the system along with the one-way reed valves used for fluid rectification. The model equations are then combined to form an overall model of the system output behavior.

#### 3.1 Mechanical Component Modeling

The piston position ( $x_p$ ) is given by

$$m_p \ddot{x}_p + b_p \dot{x}_p + k_p x_p = \alpha I - A_{\text{ch}} P_{\text{ch}}, \quad (3)$$

where  $m_p$ ,  $b_p$ , and  $k_p$  represent the effective mass, stiffness, and damping of the piston, metal diaphragm, and Terfenol-D driver.

The output cylinder position ( $x_o$ ) is defined by the differential equation

$$m_l \ddot{x}_{\text{out}} + b_l \dot{x}_{\text{out}} + k_l x_{\text{out}} = A_{\text{out}} (P_{\text{hs}} - P_{\text{ls}}) - F_f - F_{\text{ext}}, \quad (4)$$

where the mass, stiffness, and damping of the piston rod are accounted with the load properties  $m_l$ ,  $b_l$ , and  $k_l$ . The external force  $F_{\text{ext}}$  represents the weight of the load. Friction in the cylinder is modeled with a Karnopp model.<sup>14, 15</sup> Letting  $F_e$  be the net force on the cylinder,  $F_e = A_{\text{out}} (P_{\text{hs}} - P_{\text{ls}}) - F_{\text{ext}}$ , the friction force is given by

$$F_f = \begin{cases} F_d & \text{if } |v| > v_{\min} \\ F_e & \text{if } |v| \leq v_{\min} \text{ and } |F_e| < F_s \\ F_s \text{sgn}(F_e) & \text{if } |v| \leq v_{\min} \text{ and } |F_e| \geq F_s \end{cases} \quad (5)$$

where  $F_s$  and  $F_d$  are the static and dynamic friction,  $v$  is the cylinder velocity, and  $v_{\min}$  is the value used for the numerical simulation to consider the cylinder motion stopped.

### 3.2 Fluid System Modeling

Figure 7 shows the layout of the internal passages within the hydraulic manifold of the system. The fluid system passages are modeled using a lumped-parameter approach; each section of fluid passage (labeled A-H) is represented by one or more nodes which represent the passage with an equivalent resistance  $R$ , inertia  $L$ , and compliance  $C$  (Figure 8).

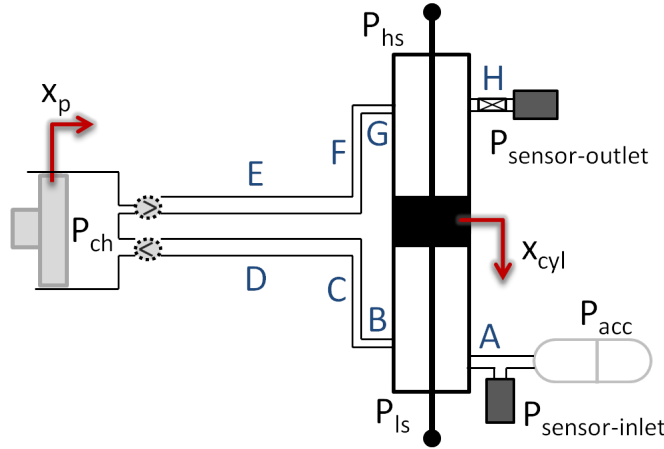


Figure 7. System model diagram showing the layout of the fluid passages.

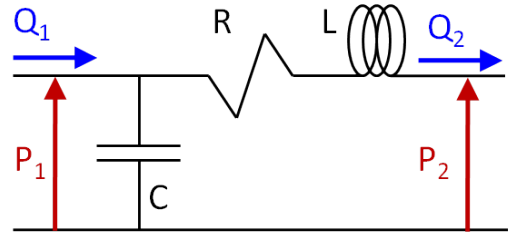


Figure 8. Each section of the fluid passages is modeled using one or more lumped-parameter nodes incorporating the equivalent resistance, inertia, and compliance of the fluid in the section.

In developing the fluid system equations, laminar flow is assumed. The Reynold's number is calculated as  $N_R = \frac{\rho D v}{\mu}$  and found to be less than 2000 indicating that the flow in the system is laminar.<sup>16</sup> The resistance term is defined by

$$R = \frac{128\mu l}{\pi d^4} \left( 1 + \frac{2.78 d}{64 l} N_R \right), \quad (6)$$

which combines the Hagen-Poiseuille law for fully-developed laminar flow (first term) with a nonlinear correction factor (second term) accounting for end-effects.<sup>17</sup> This equation can be simplified to,<sup>16</sup>

$$R = \frac{128\mu l}{\pi d^4} \left( 1 + \frac{0.1736}{\pi} \frac{\rho}{l\mu} Q \right). \quad (7)$$

The inertia ( $L$ ) and compliance ( $C$ ) terms account for the mass and stiffness of fluid contained in each lump of fluid

$$L = \frac{4\rho l}{3A}, \quad C = \frac{lA}{\beta}, \quad (8)$$

where  $\rho$  is the density of the fluid,  $l$  is the length of the fluid lump,  $A$  is the area. The bulk modulus  $\beta$  is considered to be a function of the pressure  $P$  and volume fraction of entrained air  $x$ ; this results in an effective bulk modulus

$$\beta = \left( \frac{1-x}{\beta_l} + \frac{x}{\beta_a} \right)^{-1} = \left( \frac{1-x}{\beta_l} + \frac{x}{P} \right)^{-1} \quad (9)$$

where  $\beta_l$  is the bulk modulus of the hydraulic fluid with no air. Even a small amount of entrained air is shown to have a large effect on the effective bulk modulus in the system (Figure 9); an important consequence of the pressure-dependence of bulk modulus is that the stiffness of the fluid in the hydraulic cylinder increases with applied load, as higher loads require higher pressures to produce output motions.

This results in two differential equations for the pressure  $P$  and flow  $Q$  at each node (Figure 8),

$$Q_1 - Q_2 = C \frac{dP_1}{dt}, \quad (10)$$

$$P_1 - P_2 = RQ_2 + L \frac{dQ_2}{dt}. \quad (11)$$

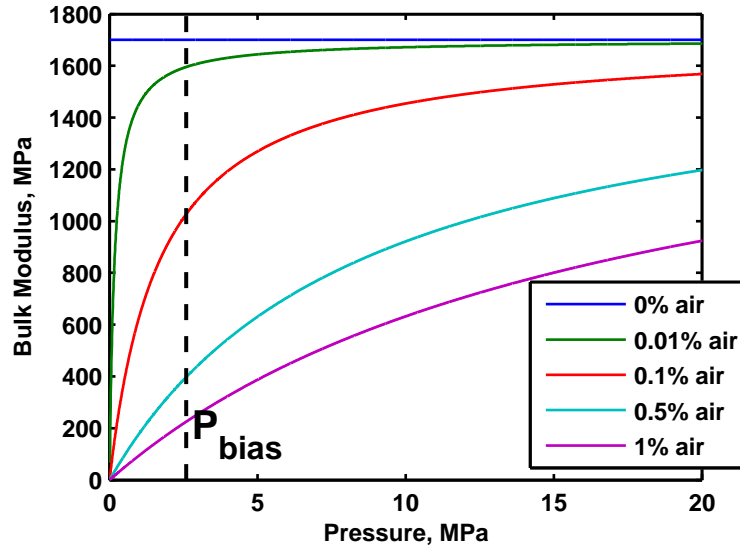


Figure 9. Variation of the effective bulk modulus of the fluid within the pump due to pressure changes and entrained air based on (9).

The larger volumes of fluid in the system, including the pumping chamber  $P_{ch}$ , high-pressure side of the output cylinder  $P_{hs}$ , and low-pressure side of the pumping chamber  $P_{ls}$ , are modeled using the fluid compliance given by the bulk modulus  $\beta$  and flow in and out of each volume:

$$\left(\frac{V_{ch}}{\beta}\right) \dot{P}_{ch} = A_p \dot{x}_p - Q_{out} + Q_{in}, \quad (12)$$

$$\left(\frac{V_{hs}}{\beta}\right) \dot{P}_{hs} = Q_G - Q_H - A_{out} \dot{x}_{out}, \quad (13)$$

$$\left(\frac{V_{ls}}{\beta}\right) \dot{P}_{ls} = Q_A - Q_B + A_{out} \dot{x}_{out}. \quad (14)$$

#### 4. REED VALVE MODELING

The opening positions of the reed tip for the output ( $x_{ro}$ ) and input ( $x_{ri}$ ) reeds are calculated by modeling the reeds as cantilever beams with equivalent mass  $m_r$ , stiffness  $k_r$ , and damping  $b_r$

$$m_r \ddot{x}_{ro} + b_r \dot{x}_{ro} + k_r x_{ro} = A_r (P_{ch} - P_{E1}), \quad (15)$$

$$m_r \ddot{x}_{ri} + b_r \dot{x}_{ri} + k_r x_{ri} = A_r (P_{D2} - P_{ch}). \quad (16)$$

The pressures  $P_{E2}$  and  $P_{D1}$  are the pressures in the manifold passages adjacent to the pumping chamber. The reed valve positions defined by (15) and (16) determine the opening area  $A_v$  of each reed valve, which has been calculated as a linear function of the tip opening  $A_v = \lambda x$  by integrating the opening area around the reed, assuming the first mode of a cantilever beam as the reed opening profile.

The pressure drop across the reeds can be modeled according to the orifice flow equation

$$\Delta P = \frac{\rho}{2} C_d^2 A_v^2 Q^2 \quad (17)$$

with discharge coefficient  $C_d = 0.61$  and reed opening area  $A_v$ .

## 5. REED VALVE DYNAMIC TESTING

Theoretical calculations of the reed frequency response by approximating the reed as a cantilever beam, indicate that the first resonance should occur at approximately 950 Hz;<sup>18</sup> this calculation includes the effect of the fluid mass on the reed response by including an added mass term

$$m_{\text{add}} = \gamma \frac{\pi}{4} w_r^2 l_r \rho, \quad (18)$$

which is the mass of fluid contained in a cylinder swept by the reed width  $w_r$  and length  $l_r$  with a correction factor  $\gamma$  to account for the relatively short aspect ratio of the reed.<sup>18</sup> To demonstrate the effect of the reed's natural frequency on the ability of the reeds to rectify fluid flow over a range of input frequencies, the resulting flow rate from a sinusoidal pressure differential was calculated using (16) and (17). The results show that the flow rate should be expected to decrease dramatically as the pressure oscillation frequency approaches the natural frequency of the reed (Figure 10). This result is expected as the response for a system vibrating at its first natural

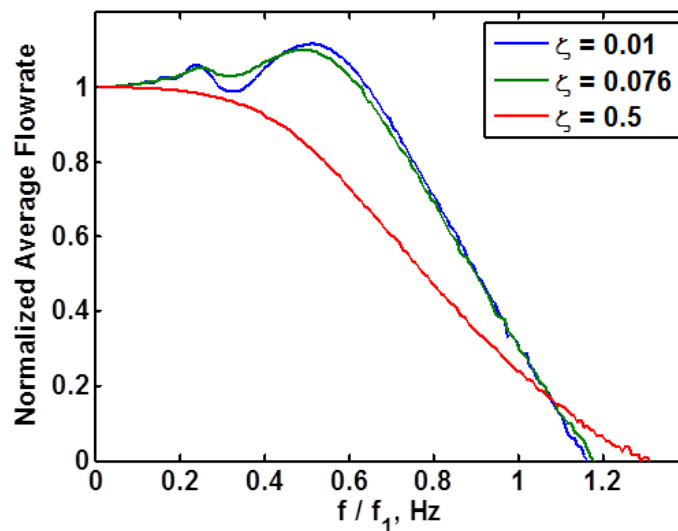


Figure 10. Normalized flow response over the reed valves for a sinusoidal pressure distribution over a range of frequencies; the flow rate decreases dramatically approaching the natural frequency of the reed.

frequency is expected to be approximately 90 degrees out of phase with the input; the reeds will therefore open and close out of phase with the fluid pressure differential at the reed natural frequency. This prediction conflicts with the experimental results (Figure 3), which have a peak in flow rate (velocity) at the reed's natural frequency.

The discrepancy between the predicted reed frequency response and the observed response from the EHA velocity experiments is due to a difference in boundary conditions between the experiment and theoretical predictions. The theoretical frequency response assumes that the reed is free to vibrate as a cantilever beam; however, in the actual pump system the reed closes against a valve seat to rectify the fluid flow. The fluid flow path contained in the reed seat presents an additional complication as the observed response does not correspond to other studies in the literature which study the effect of a cantilever beam approaching a solid wall.<sup>19</sup> In order to test the effect of the valve seat on the frequency response, a test holder was fabricated to clamp the reed against a valve seat containing a flow path with the same dimensions used in the experimental pump (Figure 11).

An additional valve was tested in a clamped-free cantilever condition for reference and to compare the test results with the theoretical calculations. The test fixture with the reed valves was excited using a shaker and the natural frequencies and mode shapes were measured using a Polytec PSV-400-M scanning laser vibrometer. The results show that the effect of the valve seat is to approximately double the natural frequency of the rod



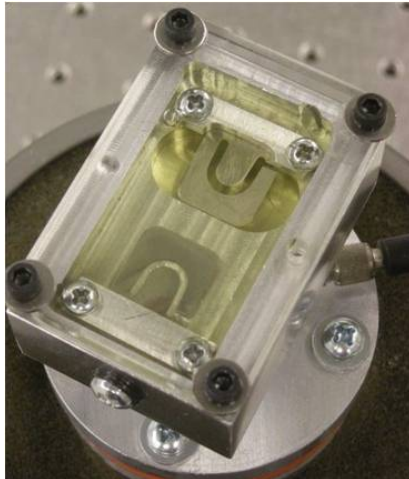


Figure 11. Test setup for evaluating the natural frequency of the reed valves; the valves are tested in the pump configuration (with valve seat, top reed) and as a cantilever beam for reference (bottom reed).

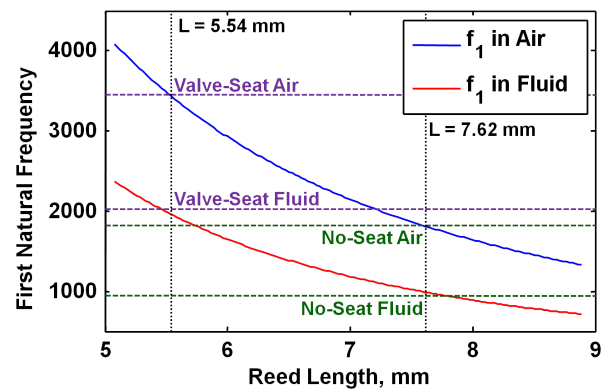


Figure 12. Reed valve dynamic experimental results compared with theoretical calculation of the natural frequency based on the length of the valve; the test results show that the effect of the reed valve seat is similar to shortening the valve from 7.62 mm to 5.53 mm.

Table 2. Reed natural frequency testing results.

Test Condition	First Natural Frequency (Hz)	Damping Ratio
No-seat in air	1820	0.05
No-seat in fluid	940	0.2
With-seat in air	3450	0.55
With-seat in fluid	2020	0.55

to 2040 Hz (Table 2). Adding the seat to the reed valve is found to effectively shorten the length of the reed valve from 7.62 mm long to 5.53 mm (Figure 12). Using this equivalent length is found to correlate well with the measured natural frequency of the reed when tested in both air and in fluid. The natural frequency of the reed in the free-cantilever condition was found to match well to the theoretical values using the actual reed length.

## 6. MODEL RESULTS

The equations for the fluid, mechanical, and reed valve subsystems were combined as a set of differential equations and solved using the MATLAB ode15s function. A list of the parameters used in the model is included in Appendix A. The model calculations show a similar double-peaked response as the experimental data (Figure 13). As the applied load is increased, the trend of the second frequency peak increasing with applied load is also demonstrated in the model due to the increased bulk modulus as a higher pressure is used to move the load.

There is some discrepancy between the magnitude of the response from the model results and the experimental data, which is most likely due to the linear model that was used for the magnetostrictive driver. The actual response of Terfenol-D varies nonlinearly with frequency and applied stress. Additionally, the input to the system over the frequency range was controlled to be a constant current. The effective field seen by the rod would be expected to decrease at higher frequencies due to losses such as eddy currents. The linear model represents an approximation of the overall behavior, which underpredicts the material response at low frequencies and over-predicts the response at high frequencies.

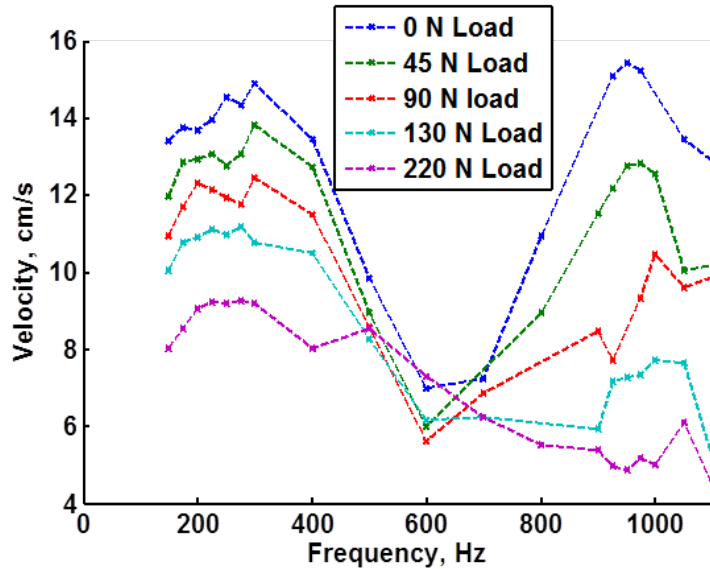


Figure 13. Model results for the calculated output velocity with a constant  $20 A_{pk-pk}$  input current over the frequency range.

## 7. SUMMARY

This paper presents a nonlinear dynamic model for a magnetostriuctive hydraulic actuator. The actuator uses one-way reed valves to rectify the high-frequency, low-displacement vibrations of a Terfenol-D rod into large motions of a hydraulic cylinder. The frequency response of the reed valves used for fluid rectification was characterized experimentally and compared to theoretical predictions; the valve seat was found to improve the frequency response by shortening the effective length of the reed. A lumped-parameter approach was used to model the fluid and mechanical components that make up the experimental actuator. Nonlinearities in the behavior of the fluid within the system, including the pressure-dependence of the bulk modulus and end-effect losses were included in the model. The experimental actuator was tested over a range of input frequencies and applied loads. A peak output power of 37 W was measured, corresponding to a measured output cylinder velocity of 17 cm/s with a 220 N applied load. The experimental results were compared with the model predictions.

## ACKNOWLEDGMENTS

Financial support for this research was provided by the member organizations of the Smart Vehicle Concepts Center, a National Science Foundation Industry/University Cooperative Research Center ([www.SmartVehicleCenter.org](http://www.SmartVehicleCenter.org)), and by The Ohio State University through a Smart Vehicle Concepts Graduate Fellowship.

## REFERENCES

1. Etrema Products, Inc., "Terfenol-D data sheet." <http://www.etrema-usa.com/documents/Terfenol.pdf> (2012). [Accessed 20 December 2012].
2. Bridger, K., Sewell, J. M., Cooke, A. V., Lutian, J. L., Kohlhafer, D., Small, G. E., and Kuhn, P. M., "High-pressure magnetostrictive pump development: a comparison of prototype and modeled performance," *Proc. SPIE* 5388, 246 (2004).
3. Larson, J. P. and Dapino, M. J., "Design of a smart material electro-hydraulic actuator with improved frequency bandwidth," *Proc. SPIE* 8343, 83430K (2012).
4. Chaudhuri, A. and Wereley, N. M., "Experimental validation of a hybrid electrostrictive hydraulic actuator analysis," *J. Vib. Acoust.* 132(2), 021006 (2010).
5. Kim, G. W. and Wang, K. W., "Enhanced control performance of a piezoelectric-hydraulic pump actuator for automotive transmission shift control," *Proc. Inst. Mech. Eng. D J. Automob. Eng.* 224(2), 161–174 (2010).

6. John, S., Sirohi, J., Wang, G., and Wereley, N. M., "Comparison of piezoelectric, magnetostrictive, and electrostrictive hybrid hydraulic actuators," *J. of Intell. Mater. Syst. and Struct.* 18(10), 1035 (2007).
7. Rupinsky, M. J. and Dapino, M. J., "Smart material electrohydrostatic actuator for intelligent transportation systems," *ASME Conf. Proc.* 2006(47683), 721–730 (2006).
8. Tan, H., Hurst, W., and Leo, D., "Performance modeling of a piezohydraulic actuation system with active valves," *Smart materials and structures* 14, 91–110 (2005).
9. Lee, D. G., Or, S. W., and Carman, G. P., "Design of a piezoelectric-hydraulic pump with active valves," *J. of Intell. Mater. Syst. and Struct.* 15(2), 107 (2004).
10. Sirohi, J. and Chopra, I., "Design and development of a high pumping frequency piezoelectric-hydraulic hybrid actuator," *J. of Intell. Mater. Syst. and Struct.* 14(3), 135–147 (2003).
11. Oates, W. S. and Lynch, C. S., "Piezoelectric hydraulic pump system dynamic model," *J. of Intell. Mater. Syst. and Struct.* 12(11), 737–744 (2001).
12. Mauck, L. D. and Lynch, C. S., "Piezoelectric hydraulic pump development," *J. of Intell. Mater. Syst. and Struct.* 11(10), 758 (2000).
13. Gerver, M. J., Goldie, J. H., Swenbeck, J. R., Shea, R., Jones, P., Ilmonen, R. T., Dozor, D. M., Armstrong, S., Roderick, R., Nimblett, F. E., et al., "Magnetostrictive water pump," *Proc. SPIE* 3329, 694–705 (March 1998).
14. Olsson, H., Åström, K., Canudas De Wit, C., Gäfvert, M., and Lischinsky, P., "Friction models and friction compensation," *Eur. J. Control* 4, 176–195 (1998).
15. Chaudhuri, A., Yoo, J. H., and Wereley, N. M., "Design, test and model of a hybrid magnetostrictive hydraulic actuator," *Smart Mater. Struct.* 18, 085019 (2009).
16. Doebelin, E., [*System Dynamics: Modeling, Analysis, Simulation, Design*], CRC (1998).
17. Merritt, H. E., [*Hydraulic Control Systems*], Wiley New York (1967).
18. Blevins, R. D., [*Formulas for Natural Frequency and Mode Shape*], Van Nostrand Reinhold Company (1979).
19. Naik, T., Longmire, E. K., and Mantell, S. C., "Dynamic response of a cantilever in liquid near a solid wall," *Sensors and Actuators A: Physical* 102(3), 240254 (2003).

## APPENDIX A. SYSTEM PARAMETERS

Tables 3 and 4 list the parameters used to model the experimental magnetostrictive hydraulic actuator.

Table 3. Fluid passage dimensions for the smart material electro-hydraulic actuator.

Fluid Passage	Diameter (cm)	Length (cm)
A	0.24	0.70
B	0.24	0.87
C	0.16	2.76
D	0.32	5.72
E	0.44	5.72
F	0.16	2.76
G	0.24	0.87
H	0.24	0.95
Low-side Sensor Passage	0.70	4.57
Inlet from Accumulator	0.95	11.43

Table 4. Magnetostrictive driver, piston, and output hydraulic cylinder properties.

Parameter	Value	Units	Description
$x$	0.02	–	Air volume fraction
$\beta_l$	1.7	GPa	Hydraulic Fluid Bulk Modulus
$E_{TD}$	15	GPa	Terfenol-D modulus
$\alpha$	233	N/A	Coupling coefficient
$m_p$	124	g	Piston effective mass
$k_p$	24.3	MN/m	Piston effective stiffness
$\zeta_p$	0.09	–	Damping ratio for the piston and driver
$m_r$	0.0206	g	Reed effective mass
$k_r$	30	N/cm	Reed effective stiffness
$\zeta_r$	0.55	–	Reed damping ratio
$\lambda$	0.85	cm <sup>2</sup> /cm	Area factor for reed tip displacement
$A_r$	0.135	cm <sup>2</sup>	Reed valve area
$A_{ch}$	5.07	cm <sup>2</sup>	Pumping chamber area
$h_{ch}$	1.27	mm	Pumping chamber height
$A_{out}$	0.95	cm <sup>2</sup>	Output cylinder area